THE JOURNAL OF BIOLOGICAL CHEMISTRY VOL. 287, NO. 46, pp. 38946–38955, November 9, 2012

The Neck Region of the C-type Lectin DC-SIGN Regulates Its Surface Spatiotemporal Organization and Virus-binding Capacity on Antigen-presenting Cells*[S]

Received for publication, May 9, 2012, and in revised form, September 25, 2012 Published, JBC Papers in Press, September 27, 2012, DOI 10.1074/jbc.M112.380121

Carlo Manzo[‡1], Juan A. Torreno-Pina[‡1], Ben Joosten[§], Inge Reinieren-Beeren[§], Emilio J. Gualda[‡], Pablo Loza-Alvarez[‡], Carl G. Figdor[§], Maria F. Garcia-Parajo[‡¶2], and Alessandra Cambi[§‖3]

From the [‡]Institut de Ciencies Fotoniques, Mediterranean Technology Park, 08860 Castelldefels (Barcelona), Spain, the [§]Department of Tumor Immunology, Nijmegen Centre for Molecular Life Sciences, Radboud University Nijmegen Medical Center, 6500 HB Nijmegen, The Netherlands, the [¶]Institució Catalana de Recerca i Estudis Avançats, 08010 Barcelona, Spain, and the [‖]Nanobiophysics Group, MIRA Institute for Biomedical Technology and Technical Medicine, University of Twente, P.O. Box 217, 7500 AE Enschede, The Netherlands

Background: Nanoclusters of the C-type lectin DC-SIGN on dendritic cells act as docking sites for viral binding.
Results: The extracellular neck region is responsible for nanocluster formation and necessary for virus binding.
Conclusion: Heterogeneous nanocluster density and spatial distribution confer broad binding capabilities to DC-SIGN.
Significance: Insights into how virus receptors preorganize and assemble into docking platforms contribute to clarifying mechanisms of virus entry.

The C-type lectin DC-SIGN expressed on dendritic cells (DCs) facilitates capture and internalization of a plethora of different pathogens. Although it is known that DC-SIGN organizes in nanoclusters at the surface of DCs, the molecular mechanisms responsible for this well defined nanopatterning and role in viral binding remain enigmatic. By combining biochemical and advanced biophysical techniques, including optical super-resolution and single particle tracking, we demonstrate that DC-SIGN intrinsic nanoclustering strictly depends on its molecular structure. DC-SIGN nanoclusters exhibited free, Brownian diffusion on the cell membrane. Truncation of the extracellular neck region, known to abrogate tetramerization, significantly reduced nanoclustering and concomitantly increased lateral diffusion. Importantly, DC-SIGN nanocluster dissolution exclusively compromised binding to nanoscale size pathogens. Monte Carlo simulations revealed that heterogeneity on nanocluster density and spatial distribution confers broader binding capabilities to DC-SIGN. As such, our results underscore a direct relationship between spatial nanopatterning, driven by intermolecular interactions between the neck regions, and receptor diffusion to provide DC-SIGN with the exquisite ability to dock pathogens at the virus length scale. Insight into how virus receptors are organized prior to virus binding and how they assemble into functional platforms for virus docking is helpful to develop novel strategies to prevent virus entry and infection.

Dendritic cells (DCs)[4] constitute a specific group of professional antigen-presenting leukocytes that link the innate and adaptive branches of the immune response by virtue of their capacity to recognize pathogen-specific structures (1). Immature DCs (imDCs) migrate from the blood into tissues, where they detect foreign antigens. Upon antigen recognition, imDCs are activated and migrate to the lymph nodes, where they present antigen-derived peptides to naive T lymphocytes and induce an effective immune response (2–4). For efficient pathogen recognition, imDCs are equipped with a large number of lectin and lectin-like receptors on the cellular membrane that bind to high mannose structures present on the surfaces of a broad range of pathogens, including viruses, bacteria, yeast, and parasites (5, 6). Because DCs can be manipulated *ex vivo*, numerous efforts have been undertaken for exploiting the extraordinary binding capabilities of lectin-like receptors to target antigens directly to DCs *in vivo*, potentially increasing the effectiveness of antitumor and antiviral vaccines (7, 8).

Dendritic cell-specific ICAM-3-grabbing nonintegrin (DC-SIGN; CD209) is a type II membrane C-type lectin receptor abundantly expressed *in vivo* on myeloid DC and macrophage populations (9, 10) as well as on *in vitro* generated monocyte-derived DCs and activated macrophages (10–12). DC-SIGN is responsible for the binding and uptake of a multitude of pathogens, such as HIV-1 (13), ebola virus (14), hepatitis C virus (15),

---

* This work was supported by Spanish Ministry of Science and Technology Grant MAT2010-19898 and Generalitat de Catalunya Grant 2009 SGR 597 (to M. F. G.-P.), Netherlands Organization for Scientific Research (NWO) Veni Grant 916.66.028 and a Human Frontier Science Program Young Investigator grant (to A. C.), and partially by an NWO TOP grant (to C. G. F.).

[S] This article contains supplemental Methods, Figs. S1–S4, and Movies 1–6.

[1] Both authors contributed equally to this work.

[2] To whom correspondence may be addressed: Institut de Ciencies Fotoniques, Mediterranean Technology Park, 08860 Castelldefels (Barcelona), Spain. E-mail: maria.garcia-parajo@icfo.es.

[3] Recipient of an NWO Meervoud subsidy. To whom correspondence may be addressed: Dept. of Tumor Immunology, Nijmegen Centre for Molecular Life Sciences, Radboud University Nijmegen Medical Center, 6500 HB Nijmegen, The Netherlands. Tel.: 31-24-361-0556; Fax: 31-24-354-0339; E-mail: a.cambi@ncmls.ru.nl.

[4] The abbreviations used are: DC, dendritic cell; imDC, immature DC; CRD, carbohydrate recognition domain; TEM, transmission electron microscopy; MF, mean fluorescence; Ab, antibody; NSOM, near-field scanning optical microscopy; STED, stimulated emission depletion; *ccdf*, complementary cumulative distribution function.

Candida albicans (16), and *Mycobacterium tuberculosis* (17) via mannan- and Lewis X oligosaccharide-dependent interactions. More recently, it has been shown that upon recognition of mannan or Lewis X carbohydrates, DC-SIGN associates with distinct signaling molecules to induce differential production of cytokines that in turn lead to enhancement or suppression of proinflammatory responses (18). The mechanisms by which these diverging signaling pathways are generated remain a mystery, although it has been suggested that the molecular structure of DC-SIGN might be altered upon binding to the two different carbohydrates.

Structurally, DC-SIGN is a tetrameric transmembrane protein, with each subunit comprising a long extracellular part with a carbohydrate recognition domain (CRD), a 7.5 tandem repeat of 23 amino acids forming the neck region, and a transmembrane part followed by a cytoplasmic tail containing recycling and internalization motifs (19–20). Analysis of recombinant molecules and hydrodynamic and surface force measurements revealed that the neck region of DC-SIGN is responsible for its tetramerization (21–23), enabling the formation of CRD multibinding sites and increasing the interaction strength with specific ligands (23). Based on these results, it has been proposed that the neck configuration is likely to play a significant role in pathogen capture (23).

Using transmission electron microscopy (TEM) and near-field optical nanoscopy, we previously showed that DC-SIGN forms nanoclusters on the membrane of fixed imDCs far beyond mere tetramerization (11, 24, 25). These results have been recently validated on living imDCs (26) and on several cell lines transfected with DC-SIGN (26, 27). Importantly, tight spatial ordering of DC-SIGN in nanoclusters resulted crucial for binding and internalization of HIV-1 (11). However, how DC-SIGN achieves such a refined level of spatial control is largely unknown. Although DC-SIGN has been shown to partially associate with lipid rafts, cholesterol extraction did not alter the integrity of the nanoclusters (11). Similarly, DC-SIGN nanocluster formation and/or stability do not require interactions with the cortical cytoskeleton (27) or association with tetraspanins (27). Recently, it has been hypothesized that large DC-SIGN domains (*i.e. microclusters*) could be formed and stabilized through interactions between the CRDs and yet unidentified extracellular components because deletion of the CRD moiety abrogated DC-SIGN microclustering (28). However, because these experiments were performed using diffraction-limited confocal microscopy, it is not clear whether the *nanoclustering* capacity of DC-SIGN also requires the presence of the CRD. Thus, despite the importance of DC-SIGN nanoclustering in pathogen recognition, the studies performed so far have not yet provided conclusive evidence to explain the origin for this well defined organization.

Here we combined biochemical assays, superresolution optical nanoscopy, single particle tracking, and Monte Carlo simulations of different DC-SIGN mutants to elucidate the mechanisms leading to DC-SIGN nanoclustering and to correlate their role with viral binding capacity. Our results reveal that homophilic interactions mediated by the neck region of DC-SIGN are responsible for its nanoclustering and enhanced virus-binding ability.

EXPERIMENTAL PROCEDURES

Cells and DNA Constructs—CHO cell lines stably expressing DC-SIGN-wt, -ΔCRD, -Δ35, and -ΔRep were established by Lipofectamine™ 2000 transfection. Human imDCs were generated from buffy coats of healthy donors as reported previously (29). Plasmids used in this study were pcDNA-3 carrying the DC-SIGN-wt or deletion mutants. These constructs have a short C-terminal AU-1 tag and were constructed as already published (30).

Binding Assays—Binding of CHO cells to soluble Alexa647-mannan was performed as follows. 50,000 cells were incubated with 50 μg/ml Alexa647-mannan in 20 mM Tris, pH 8.0, containing 150 mM NaCl, 1 mM $CaCl_2$, 2 mM $MgCl_2$, and 1% BSA (TSA buffer) for 30 min on ice in the presence or absence of 20 μg/ml anti-DC-SIGN blocking mAb (AZN-D1) or 100 μg/ml unlabeled mannan. After thorough washing in PBS, the percentage of cells that had bound mannan was detected by flow cytometry using the FACSCalibur™ flow cytometer (BD Biosciences). The values represent the mean ± S.D. of duplicates of one representative experiment of three. Binding to gp120-coated beads was performed as already reported (11). Briefly, streptavidin-modified TransFluorSpheres (505/515 nm, 40-nm diameter; Molecular Probes) were coated with recombinant biotinylated gp120 (HIV-1 III B; ImmunoDiagnostics, Inc., Woburn, MA) and were added to 50,000 cells in a ratio of 20 beads/cell in TSA buffer, and the suspension was incubated for 30 min at 37 °C. When necessary, cells were preincubated with 20 μg/ml blocking mAb or 2 mM EDTA for 10 min at room temperature. Binding was determined by measuring the percentage of cells that have bound fluorescent beads by flow cytometry. Binding to FITC-conjugated zymosan was performed as already described (16). Briefly, CHO transfectants were incubated with FITC-labeled zymosan particles in the absence or the presence of mannan (100 μg/ml) or anti-DC-SIGN mAb AZN-D1 (20 μg/ml) in TSA buffer. After 30 min of incubation at 37 °C, cell-zymosan conjugates were analyzed by flow cytometry, and the percentage of CHO cells that had acquired an FITC+ signal was quantified by flow cytometry.

Antigen Internalization Assay—The internalization assay was performed as already reported (31). Briefly, CHO cell lines stably expressing DC-SIGN wild type or the deletion mutants were incubated with anti-DC-SIGN mAb hD1 (5 μg/ml) in serum-free medium for 20 min on ice. After washing the unbound mAb in ice-cold medium, half of the cells were further incubated for 15 min on ice to prevent internalization, whereas the other half was shifted to 37 °C for 15 min to induce internalization. Subsequently, cells were placed back on ice to stop internalization, washed in ice-cold PBS containing 3% BSA, and incubated with phycoerythrin-conjugated goat anti-human antibodies for 20 min on ice to stain the mAb still present at the cell surface. Unbound Abs were washed away, and cells were fixed in 1% formaldehyde. The mean fluorescence (MF) of the samples was measured by flow cytometry, and the percentage of internalized mAb was calculated as ((MF at 37 °C − MF at 4 °C)/MF at 4 °C) × 100. The normalization to the fluorescence intensity at the steady state (4 °C) prevents oscillations in the expression levels from affecting the percentage of internalization. Isotype controls were always included.

Gold Labeling of Whole-mount Samples—CHO transfectants were allowed to adhere and spread on glass coverslips covered by a thin layer of Formvar for 1 h at 37 °C and immediately fixed with 1% paraformaldehyde for 15 min. After two washing steps with PBS and a subsequent incubation (60 min at room temperature) with blocking buffer (PBS, 0.1% glycine, 1% BSA, and 0.25% gelatin) to reduce specific background, the specimens were incubated for 30 min with primary antibodies (DCN46 Ab (Pharmingen) for DC-SIGN-wt, -ΔCRD, and -Δ35 or anti-AU1 Ab (Covance) for DC-SIGN-ΔRep) in blocking buffer on ice, rinsed in PBS, and fixed in 1% paraformaldehyde and 0.1% glutaraldehyde for 15 min. After two washing steps with PBS and blocking buffer, the samples were incubated with rabbit anti-mouse IgG (to detect mAb) for 30 min on ice. A final incubation with 10-nm diameter gold-labeled Protein A (to detect polyclonal antibodies) was performed, followed by final fixation in 1% glutaraldehyde in phosphate buffer for 20 min at room temperature.

To exclude the possibility that the observed difference in nanoclusters was not an artifact of the Ab chosen, anti-AU1 as well as anti-DC-SIGN AZN-D1 and DCN46 antibodies have been used for labeling and comparing DCSIGN wild type and the different mutants. More specifically, whereas anti-AU1 Ab was used to label all DC-SIGN molecules (because all constructs bear the AU1 tag), the anti-CRD Ab AZN-D1 was used to label all DC-SIGN molecules except the Δ-CRD mutant, and the anti-neck Ab DCN46 was applied to label all DC-SIGN molecules except the Δ-Repeat mutant (31, 32). When anti-AU1, AZN-D1, and DCN46 labeling were compared for the DC-SIGN wild type, no significant differences in the nanoclustered organization of this receptor were observed (see supplemental Fig. S1).

Digital TEM images were processed by custom-written software based on Matlab. See the supplemental Methods text for a full description of sample imaging and analysis.

Sample Preparation for Superresolution Nanoimaging—CHO and imDC cells were plated on glass coverslips and fixed with 4% paraformaldehyde and 0.2% glutaraldehyde for 2 h at room temperature. After blocking of the Fc receptors with 2% human serum, the cells were stained with 30 nM DCN46 Ab (Pharmingen) or anti-AU1 Ab (Covance) for 30 min at room temperature. Secondary Ab labeling was performed with 30 nM Alexa Fluor 488-labeled goat anti-mouse Ab (Invitrogen) for 30 min at room temperature. Washing steps were performed with cold PBS buffer (1×). Isotype controls were performed in every experiment in order to rule out nonspecific Ab binding.

Superresolution images of DC-SIGN on fully intact cell membranes were obtained using a commercial CW-STED system (Leica Microsystems) or a custom confocal/near-field scanning optical microscopy (NSOM) set-up. Brightness and spot sizes from multiple images were extracted using a custom-written software based on Matlab. See the supplemental Methods for a full description of sample preparation, imaging, and analysis.

Single Qdot Tracking—CHO and imDC cells were stained at sublabeling conditions with anti-human DC-SIGN Fab fragments, generated from DCN46 mAb or monovalent anti-human AU1 antibodies. The Fab fragments and the monovalent antibodies were biotinylated and linked to streptavidin-coated quantum dots (Qdot655, Invitrogen). Samples were imaged using a custom-made single molecule epimicroscope. Movies were recorded on the upper side of the cell membrane at 30–60 Hz frame rates. A full description of the sample preparation, experimental procedure, and trajectory analysis is provided in the supplemental Methods.

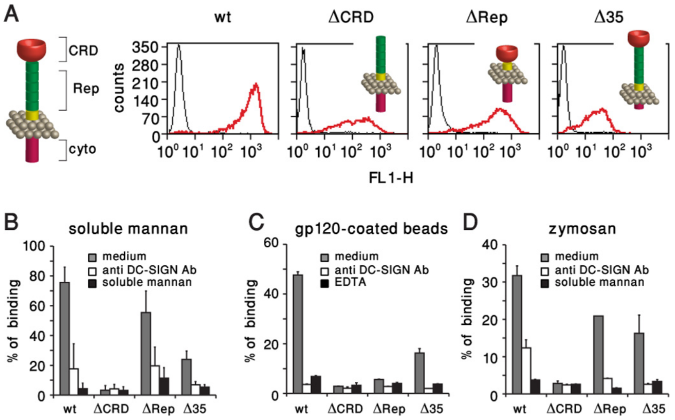

FIGURE 1. **Mutated DC-SIGN forms are functional but have impaired virus-binding capacity.** *A*, schematics of DC-SIGN-wt and cell surface expression levels of DC-SIGN-wt and mutants on stably transfected CHO cells as determined by FACS analysis. The *black histogram* represents the isotype control, and the *red histogram* indicates the specific staining with anti-DC-SIGN Ab (anti-AU1). *B–D*, binding of soluble fluorescent Alexa647-mannan (*B*), gp120-coated fluorescent nanobeads (40 nm Ø) (*C*), and micrometer-sized FITC-zymosan (*D*) to CHO cells expressing DC-SIGN-wt or mutants was measured by FACS. Specificity was determined by measuring binding in the presence of anti-DC-SIGN blocking Ab (AZN-D1) or Ca^{2+}-chelating agent EDTA or soluble non-fluorescent mannan. One representative experiment of three is shown. Values represent the average of duplicate experiments with corresponding S.D. (*error bars*).

RESULTS

Mutated DC-SIGN Forms Are Functional but Have Impaired Virus-binding Capacity—We previously showed that DC-SIGN expressed in CHO cells serves as a valid model system to study binding, internalization, and trafficking of different antigens targeted to DC-SIGN, recapitulating its essential activities on imDCs (33, 34). We thus produced three different DC-SIGN mutants by deletion of specific regions and stably transfected them in CHO cells to investigate their effect on pathogen binding (Fig. 1*A*). The mutants are denoted as ΔCRD (lacking the CRD domain), ΔRep (lacking the tandem repeats in the extracellular neck region), and Δ35 (lacking the first 35 amino acids from the N terminus in the cytoplasmic tail). We evaluated the functionality and binding capability of the stable transfectants to soluble ligands and virus-sized and micrometer-sized objects. Whereas DC-SIGN-wt, -ΔRep, and -Δ35 bind to fluorescent soluble mannan, the lack of the CRD expectedly prevents binding, consistent with the fact that DC-SIGN-mediated interactions occur through the CRD (20) (Fig. 1*B*). The addition of blocking antibodies or competing soluble mannan significantly reduces the binding in all cases, showing DC-SIGN specificity. These results confirm that DC-SIGN-wt, -ΔRep, and -Δ35 are all functional on CHO cells and further-

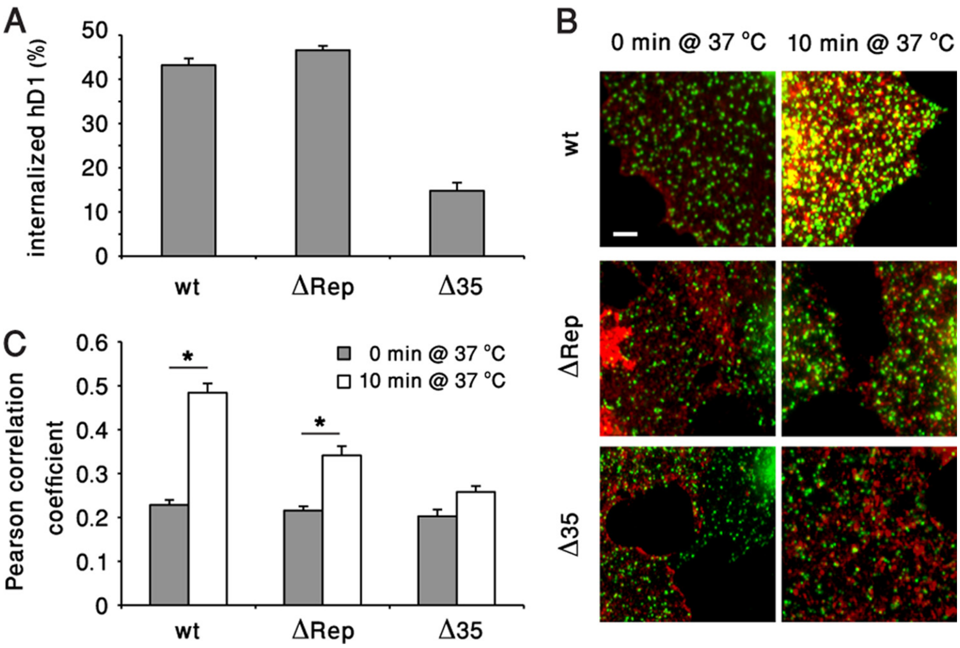

FIGURE 2. **The cytoplasmic tail impacts on DC-SIGN clathrin-dependent internalization.** *A*, CHO cells stably transfected with DC-SIGN constructs were incubated with anti-DCSIGN mAb hD1 at 4 °C, washed, and incubated for 30 min at 37 °C to induce endocytosis. After staining with a fluorescent secondary Ab, the samples were analyzed by flow cytometry. The percentage of internalization was calculated as indicated in the supplemental Methods. One representative experiment performed in triplicate of three is shown. *B*, CHO transfectants were incubated with hD1 at 4 °C, washed, and briefly incubated with isotype-specific Alexa647 (*red*)-conjugated secondary Abs at 4 °C. After washing, cells were kept on ice (0 min at 37 °C) or shifted for 10 min at 37 °C to induce endocytosis (10 min at 37 °C). After fixation and permeabilization, clathrin (*green*) was labeled, and the sample was analyzed by confocal microscopy on a Leica DMRA fluorescence microscope equipped with a COHU CCD camera. The *pictures* are *enlarged areas* taken from representative cells. *Scale bar*, 5 μm. *C*, Pearson colocalization coefficient plot of DC-SIGN and clathrin. Values ± S.E. (*error bars*) are the average of multiple images from several cells in at least three different experiments. *, $p < 0.01$, *t* test.

more show that the CRD is available for binding even in the absence of the neck region.

To investigate the DC-SIGN capability for virus docking, we carried out binding assays to gp120-coated nanobeads (40 nm in diameter; Fig. 1*C*) having a size comparable with HIV-1 (35). Interestingly, significant binding is only observed on DC-SIGN-wt and -Δ35. Although a lack of binding is expected for DC-SIGN-ΔCRD, the complete absence of binding of DC-SIGN-ΔRep indicates a key role for the neck region in securing interactions with nanometer-sized particulate antigens. This was further confirmed by using real HIV-1 virus particles, which were bound by CHO cells expressing DC-SIGN-wt and not by DC-SIGN-ΔRep (supplemental Fig. S4), thus validating the use of nanobeads as virus-like particles and in agreement with previous studies from our and other laboratories (30, 34). To further investigate the capability of binding to large objects, we performed similar experiments using micrometer-sized zymosan particles (yeast cell walls; Fig. 1*D*). High binding was retrieved for DC-SIGN-wt and all of the mutants, except for DC-SIGN-ΔCRD, in similar fashion as found for the soluble ligand. Note that the somewhat lower binding of DC-SIGN-Δ35 in all cases is due to its lower expression level as compared with -wt, -ΔCRD, and -ΔRep (Fig. 1*A*). These results show that whereas binding of DC-SIGN and its mutants to soluble ligands and large particles occurs with similar efficiency, the neck region of DC-SIGN is crucial to ensure binding of small virus-sized particles.

The Cytoplasmic Tail Impacts on DC-SIGN Clathrin-dependent Internalization—We previously showed that DC-SIGN-mediated endocytosis of virus-like particles occurs via clathrin (33, 34). Therefore, we sought to investigate the effect of structural mutations on DC-SIGN-mediated endocytosis. Truncation of the neck region (DC-SIGN-ΔRep) does not affect antigen internalization compared with DC-SIGN-wt (Fig. 2*A*). In contrast, deletion of the cytoplasmic tail (DC-SIGN-Δ35) significantly reduced internalization (Fig. 2*A*), supporting previous findings obtained on DC-SIGN-Δ35 expressed on Raji cells and incubated with HIV-1 virions (36). Subsequently, we used confocal imaging to determine the degree of colocalization of anti-DC-SIGN mAbs and clathrin before and 10 min after endocytosis triggering (Fig. 2*B*). Colocalization with clathrin was not observed for DC-SIGN-wt or the two mutants investigated (DC-SIGN-ΔRep and DC-SIGN-Δ35) in the basal state. Triggering of endocytosis by shifting the temperature to 37 °C for 10 min induced significant colocalization with clathrin for DC-SIGN-wt and DC-SIGN-ΔRep but not for DC-SIGN-Δ35, as quantified using the Pearson correlation coefficient (Fig. 2*C*). Our data thus show that the cytoplasmic tail of DC-SIGN is crucial for clathrin-dependent endocytosis, whereas the neck region has no major influence on internalization.

The Neck Region Is Required for DC-SIGN Nanoclustering—It is known that DC-SIGN forms nanoclusters on the cell surface of imDCs and of several cell lines (11, 24–27). To investigate whether a potential relationship might exist between the molecular structure of DC-SIGN and its nanoclustering capacity, we performed TEM on whole-mount samples of CHO cells (Fig. 3*A*). TEM images of immunogold-labeled DC-SIGN-wt showed a non-homogeneous receptor distribution over the cell membrane, characterized by regions of closely grouped particles (Fig. 3*A*, *top*). Similar nanoclustered organization was

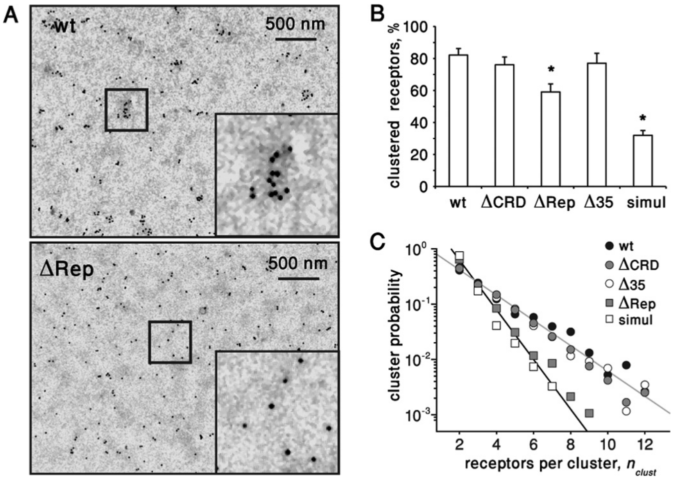

FIGURE 3. **Truncation of neck region affects DC-SIGN nanoclustering.** *A*, representative TEM images of whole-mount, immunogold-labeled CHO cells expressing DC-SIGN-wt (*top*) and DC-SIGN-ΔRep (*bottom*). Anti-AU1 mAb and 10-nm Ø gold particles were used to specifically stain DC-SIGN. Results are representative of multiple cells in several independent experiments. *B*, the digital images of electron micrographs were processed by custom-written software based on Matlab (see supplemental Methods) to extract the percentage of DC-SIGN molecules organized in nanoclusters for DC-SIGN-wt and the different mutants (-ΔCRD, -ΔRep, and -Δ35). The results are compared with simulations of random organization with similar surface density as in the experiments. A *t* test was used to compare the data of DC-SIGN-wt with DC-SIGN-ΔCRD data and to compare DC-SIGN-Δ35 data with DC-SIGN-ΔRep data (*, $p < 10^{-5}$). *C*, probability distribution of the number of particles per nanocluster from multiple TEM images over at least three independent experiments compared with simulation of random distribution with the same surface density as in the experiments. *Lines* are guides for the eye. At least 10 different TEM images over different cells are shown at each condition. *Error bars*, S.D.

found for the ΔCRD and the Δ35 mutants (supplemental Fig. S2). In contrast, a significantly more disperse distribution was observed for the ΔRep mutant (Fig. 3*A*, *bottom*). We analyzed the images by means of a cluster-searching algorithm that discriminates between isolated and clustered receptors by recursively comparing the interparticle distances with a threshold value of 80 nm (see supplemental Methods and Fig. S3). Quantification of the DC-SIGN-wt, -ΔCRD, and -Δ35 gold particle distributions showed that the large majority (~80%) of receptors are organized in nanoclusters and that this percentage drops to ~60% for DC-SIGN-ΔRep (Fig. 3*B*). Because two particles closer than 80 nm from each other are already defined as a cluster by the algorithm (supplemental Fig. S3 and supplemental Methods), we further inquired whether the degree of clustering of DC-SIGN-wt differed from that of the mutants. For this, we calculated the distribution of the number of particles per nanocluster (n_{clust}). The cluster probability distributions are similar for DC-SIGN-wt, -ΔCRD, and -Δ35, indicating that the CRD and the cytoplasmic tail of DC-SIGN do not play a role in DC-SIGN nanoclustering (Fig. 3*C*). In remarkable contrast, the large majority of the DC-SIGN-ΔRep nanoclusters contain at the most 2–3 particles (Fig. 3*C*). Beyond these values, the distribution of cluster sizes decays very rapidly, significantly overlapping with that of simulations of random organization. Indeed, the probability of finding clusters of four particles is nearly 6-fold lower in the case of DC-SIGN-ΔRep with respect to DC-SIGN wild type (and the other mutants) and 10-fold lower for clusters larger than eight particles (Fig. 3*C*). Altogether, these data demonstrate that deletion of the neck region severely reduces the aggregation state of DC-SIGN at the nanoscale, indicating that the neck region is crucial to maintain nanocluster integrity.

Superresolution Optical Nanoscopy Reveals Differences in the Spatial Organization of DC-SIGN That Depend on Its Molecular Structure—Although TEM shows the presence of DC-SIGN nanoclustering on CHO cells, in a similar fashion as already reported for imDC (11), steric hindrance between Abs and/or gold beads can induce non-saturated receptor labeling, potentially leading to an underestimation of nanoclustering. Therefore, to confirm DC-SIGN-wt nanoclustering and its abrogation for DC-SIGN-ΔRep, we performed extensive nanoscale imaging on fully intact CHO cells and imDCs using stimulated emission depletion (STED) as well as NSOM (see supplemental Methods).

Representative confocal and STED images of DC-SIGN-wt on the membrane of fixed CHO cells are shown in Fig. 4, *A* and *B*. With an optical resolution of 95 nm, STED reveals individual DC-SIGN spots well separated on the cell membrane and significantly brighter than those on the glass substrate, which arise from sparsely and nonspecifically attached individual antibodies (Fig. 4*B*). Similar results were obtained when imaging DC-SIGN on monocyte-derived imDCs using a combined single molecule confocal/NSOM set-up at an optical resolution of 90 nm (Fig. 5, *A* and *B*) (24, 25). In contrast, significantly weaker florescent spots were retrieved when performing STED imaging of DC-SIGN-ΔRep on CHO cells (Fig. 4, *C* and *D*). The physical size of the spots was determined from multiple superresolution images by directly measuring their full width at half-maximum (Fig. 4*E*). In full agreement with our TEM data, the size distribution of DC-SIGN-ΔRep spots markedly shifted toward smaller diameters compared with DC-SIGN-wt, being similar in size to the STED resolution (Fig. 4*E*, *inset*), consistent with a strong reduction of nanoclustering or its complete abrogation. On the other hand, fluorescent spots of DC-SIGN-wt on CHO cells and endogenous DC-SIGN on imDCs exhibited similar average sizes (~180 nm) and comparable size distributions (Fig. 5, *C* and *D*). Brightness analysis (see supplemental Methods) to estimate the number of molecules per fluorescent spot confirmed nanoclustering of DC-SIGN-wt with a mean value of 7.5 (S.D. = 2.7) molecules/nanocluster. This value reduced to 1.8 (S.D. = 0.8) in the case of DC-SIGN-ΔRep. Collectively, these results confirm that the neck region of DC-SIGN crucially affects its nanocluster capacity. Because the neck region is also imperative for DC-SIGN tetramerization (21, 37), our data indicate that intermolecular interactions mediated by the neck region of DC-SIGN regulate different hierarchical levels of receptor spatial organization on the cell membrane. Together with the reduced binding capability to virus-sized particles observed for DC-SIGN-ΔRep, our data establish a direct relationship between nanoclustering formation and the exquisite ability of DC-SIGN to dock pathogens at the virus length scale.

DC-SIGN Nanoclusters Are Mobile on CHO Cells and imDCs—Recent reports on DC-SIGN expressed on NIH-3T3 cells and imDC showed an unusual stability of DC-SIGN in terms of dynamics (26–28). We decided to thoroughly investigate the lateral mobility of DC-SIGN on both CHO and imDCs

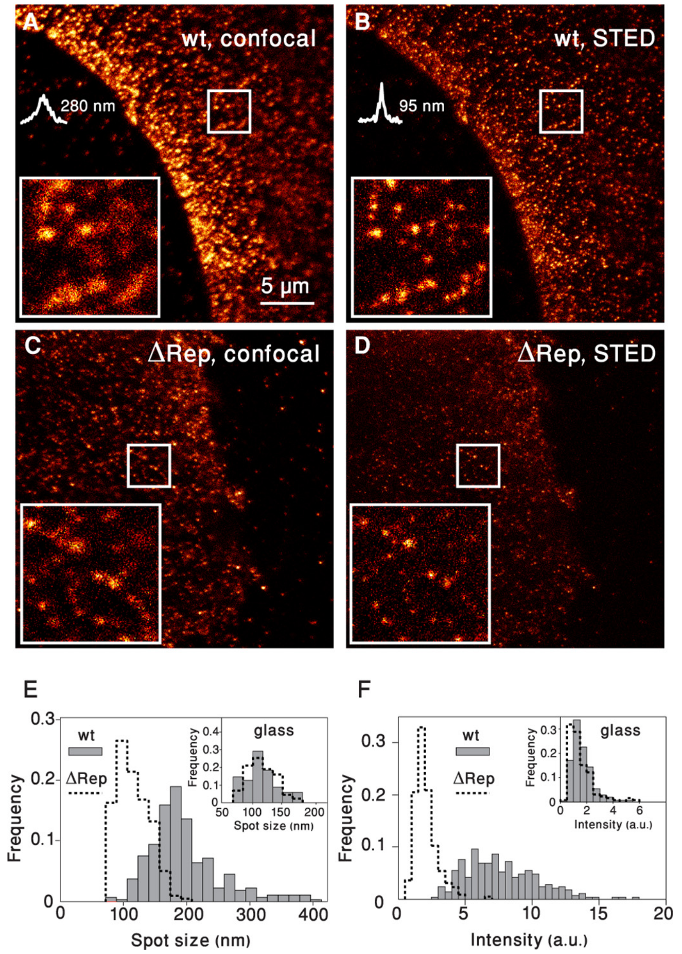

FIGURE 4. **Superresolution optical nanoscopy confirms loss of nanoclustering for DC-SIGN-ΔRep.** *A–D*, confocal (*A* and *C*) and counterpart STED (*B* and *D*) images of DC-SIGN-wt (*A* and *B*) and DC-SIGN-ΔRep (*C* and *D*) on CHO cells. The *insets* highlight the increased resolution of STED compared with diffraction-limited confocal microscopy. Images were obtained on a CW-STED system (Leica Microsystems), with a ×100/1.4 numerical aperture oil immersion objective (HCX PL APO, Leica Microsystems). *E*, normalized distribution of the spot sizes obtained for DC-SIGN-wt (*gray bars*) compared with that of DC-SIGN-ΔRep (*dotted area*). The average spot sizes are 186 nm (55 nm) and 108 nm (24 nm) for DC-SIGN-wt and -ΔRep, respectively. The *inset* shows the spot sizes obtained from individual Abs nonspecifically attached to glass and are used to illustrate the spatial resolution of STED (~100 nm). *F*, normalized intensity distribution of fluorescent spots obtained for DC-SIGN-wt (*gray bars*) compared with that of DC-SIGN-ΔRep (*dotted area*). The *inset* shows the corresponding intensity of spots found on glass. Shown are 266 and 198 spots of DC-SIGN-wt and -ΔRep, respectively, from multiple STED images.

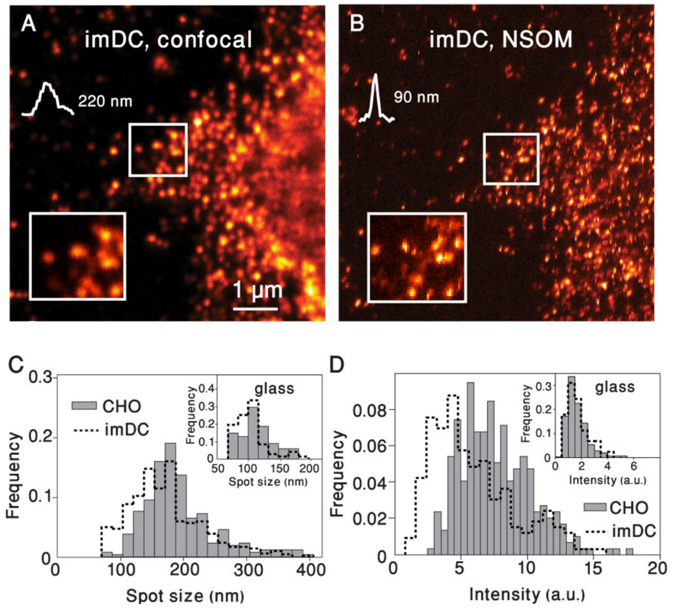

FIGURE 5. **NSOM confirms DC-SIGN nanoclustering on imDC.** *A* and *B*, confocal (*A*) and counterpart NSOM (*B*) images of DC-SIGN on imDC. The *insets* highlight the increased resolution of NSOM compared with diffraction-limited confocal microscopy. Images were obtained on a custom-built NSOM/confocal microscope (Zeiss Axiovert), with a ×100/1.3 numerical aperture oil immersion objective (Zeiss). *C*, normalized distribution of the spot sizes obtained for DC-SIGN on imDC (*dotted area*) compared with that of CHO cells expressing DC-SIGN-wt (*gray bars*). The *inset* shows the spot sizes obtained from individual Abs nonspecifically attached to glass and are used to illustrate the spatial resolution of NSOM (~100 nm). *D*, normalized intensity distribution of fluorescent spots obtained for DC-SIGN on imDC (*dotted area*) compared with that of CHO cells expressing DC-SIGN-wt (*gray bars*). The *inset* shows the corresponding intensity of spots found on glass.

using particle tracking (SPT) of quantum dots (Qdot) specifically labeling DC-SIGN, at high speed (60 frame/s) and 20-nm localization accuracy. To avoid potential artifacts due to interactions between the cell ventral membrane and the substrate, we performed Qdot labeling of DC-SIGN (either using biotinylated anti-DC-SIGN DCN46 Fab or anti-AU1 single-chain Ab) after cell stretching and recorded individual trajectories exclusively on the dorsal membrane. Clear mobility of DC-SIGN-wt nanoclusters and DC-SIGN-ΔRep was observed on CHO cells (Fig. 6*A* and supplemental Movies 1–4) in apparent contrast to the results obtained on NIH-3T3 cells (27, 28).

To quantify the degree of mobility of DC-SIGN, we built individual trajectories from multiple movies and generated plots of the mean squared displacement as a function of time lag. Apparent diffusion coefficients D_{2-4} were calculated from the initial slopes by linear fit from the second to the fourth point and included in a semilog plot (Fig. 6*B*). The D_{2-4} values of DC-SIGN-wt nanoclusters varied from 10^{-3} to 10^{-1} $\mu m^2/s$, with a median value of $D_{2-4} = 6.5 \times 10^{-2}$ $\mu m^2/s$. On the other hand, the D_{2-4} distribution of DC-SIGN-ΔRep was significantly narrower and shifted to larger D_{2-4} values, with a median value of $D_{2-4} = 1.23 \times 10^{-1}$ $\mu m^2/s$. Because the diffusion coefficient D depends on the size of the diffusing object R as $D \propto 1/R$, the higher D_{2-4} values observed on DC-SIGN-ΔRep compared with those of DC-SIGN-wt are entirely consistent with nanocluster dissolution (38, 39).

To validate our results on CHO cells, we performed single Qdot tracking of endogenous DC-SIGN nanoclusters on monocyte-derived imDCs. Apparent mobility was also observed on the dorsal membrane of imDCs (Fig. 6*A* and supplemental Movies 5 and 6), with D_{2-4} values comparable with those obtained for DC-SIGN-wt on CHO cells (Fig. 6*C*). Because D_{2-4} does not report on the long term diffusion behavior we then generated cumulative mean squared displacement plots of all trajectories at longer time lags for DC-SIGN-wt, DC-SIGN-ΔRep on CHO, and DC-SIGN on imDCs (Fig. 6*D*). In all the three cases, the plots are nearly linear, indicating Brownian diffusion of DC-SIGN on both imDCs and CHO cells. As expected, the average D value of DC-SIGN-ΔRep, as extracted from the slope of the cumulative mean squared displacement plot, is higher than that of DC-SIGN-wt. Moreover, the immobile fraction ($D < 6 \times 10^{-4}$ $\mu m^2/s$) of DC-SIGN in the

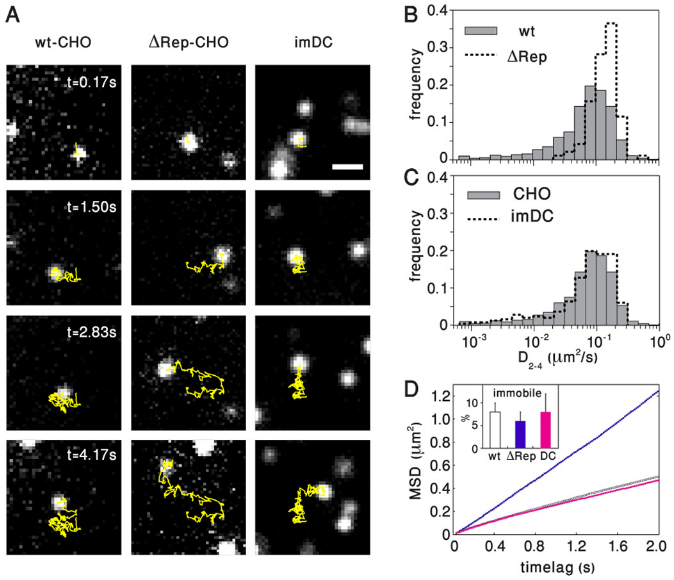

FIGURE 6. **DC-SIGN nanoclusters are freely mobile on CHO cells and imDCs.** *A*, selected sample time series of DC-SIGN-Qdots to illustrate the mobility of DC-SIGN-wt (*left*), DC-SIGN-DRep (middle), and DC-SIGN on imDC (*right*) (see supplemental Movies 1–6). *Scale bar*, 1 μm. Experiments were performed using a custom single-molecule sensitive epifluorescence microscope equipped with a ×63/1.2 numerical aperture water immersion objective (Olympus) and an EM-CCD camera (Hamamatsu). *B*, normalized semilog distribution of D_{2-4} values at short time lags for DC-SIGN-wt (*gray bars*) and DC-SIGN-ΔRep (*dotted area*). Each histogram contains at least 100 trajectories taken from >50 cells in multiple experiments. *C*, normalized semilog distribution of D_{2-4} values at short time lags for DC-SIGN-wt (*gray bars*) and DC-SIGN on imDC (*dotted area*). At least 250 trajectories/histogram from >40 cells in multiple experiments were analyzed. *D*, cumulative mean squared displacement plots of DC-SIGN-wt (*black*), DC-SIGN-ΔRep (*blue*), and DC-SIGN on imDC (*magenta*). The *inset* shows the percentage of trajectories with $D_{2-4} < 6 \times 10^{-4}$ $\mu m^2/s$ and classified as immobile. *Error bars*, S.D.

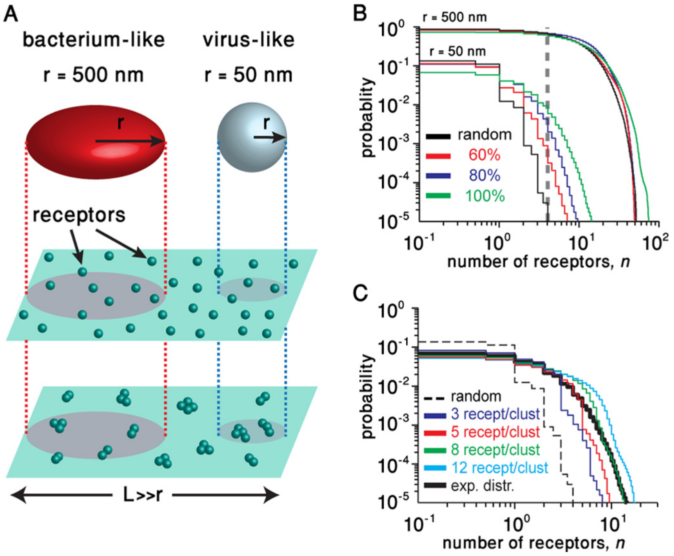

FIGURE 7. **Monte Carlo simulations show the effect of nanoclustering on pathogen binding.** *A*, schematics of the simulation of pathogen landing over a cell membrane containing receptors spatially distributed in a random or clustered fashion. *B*, complementary cumulative distribution function (*ccdf*) for having a given number of receptors at the pathogen-cell interface for two pathogen radii (50 and 500 nm) at different degrees of nanoclustering (*black*, random distribution; *red*, 60% clustering; *blue*, 80% clustering; *green*, full clustering). *C*, *ccdf* for having a given number of receptors at the pathogen-cell interface for different cluster densities. The *thick black line* denotes the experimental distribution.

three cases accounted for <10% of all trajectories analyzed. These results thus conclusively confirm lateral mobility of DC-SIGN nanoclusters within the cell membrane and further evidence a faster diffusion of DC-SIGN-ΔRep fully consistent with nanocluster dissolution at the cell membrane.

Monte Carlo Simulations Indicate That DC-SIGN Nanoclustering Enhances Viral Binding Ability—Because the decreased capability of DC-SIGN-ΔRep to bind to virus-sized particles correlated with a loss of nanoclustering on the cell membrane, we wished to understand the impact of receptor organization and, in particular, the role of DC-SIGN nanoclustering on viral binding. For this, we turned to Monte Carlo simulations, where we considered different degrees of receptor organization and allowed pathogens of different sizes to land on the cell membrane. We first sought to investigate the role of receptor clustering as a function of pathogen size by choosing two extreme cases (*i.e.* pathogens with sizes comparable with those of viruses ($r = 50$ nm) and pathogens with sizes comparable with those of bacteria ($r = 500$ nm)) (Fig. 7*A*). As schematically depicted in Fig. 7*A*, pathogens are approximated as spheres of radius r and the membrane as a flat square region with lateral size $L \gg r$. Receptor molecules are positioned on the membrane according to different spatial distributions, varying the degree of clustering, from completely random to fully clustered. In the simulations, the pathogen lands at a random position on the cell membrane, and the number of DC-SIGN receptors (n) within the area projected by the pathogen is counted. From these data, the complementary cumulative distribution function (*ccdf*) is obtained and plotted *versus n*. The *ccdf* value for a given n represents the probability that at least n receptors are accessible to the pathogen at the moment of membrane contact. This quantity is important for pathogen binding because the larger the number of accessible receptors n, the more likely it is for ligands on the pathogen surface to engage specific bonds with the membrane receptors.

First, we investigated the effect of receptor nanoclustering on virus binding ($r = 50$ nm) while keeping constant the total receptor density. As the percentage of clustering is increased, the *ccdf* decays at higher n, indicating an increased probability of having more accessible receptors around the virus contact point (Fig. 7*B*). Taking as a reference the value of $n = 4$ (*dashed vertical line*), the corresponding *ccdf* varies over more than 2 orders of magnitude as a function of the clustering percentage, from $<10^{-4}$ for random organization, to $\sim 10^{-2}$ for total clustering. Importantly, a slight increase in clustering percentage from 60 to 80%, similarly to what is observed in the TEM images for DC-SIGN-ΔRep and -wt, respectively, already produces a 5-fold probability enhancement.

Although a qualitatively similar effect is also visible for larger pathogen-like particles ($r = 500$ nm), the increased clustering induces a much smaller variation. Indeed, a change from random distribution to 80% clustering induces at most a 5-fold increase in the *ccdf* ($n = 30$), and a significant change is only observed in the case of total clustering for $n > 40$. Our simulations thus confirm that nanoclustering has a crucial role for the docking of virus-sized particles and provides a mechanistic explanation for the distinct binding capabilities of DC-SIGN by correlating pathogen size with DC-SIGN spatial organization.

Heterogeneity in Cluster Density Confers Broader Binding Capability to DC-SIGN—TEM and superresolution images showed that DC-SIGN organizes in nanoclusters having a broadly distributed size and number of particles (Figs. 3*C* and 4, *E* and *F*). To inquire whether this multidispersed distribution offers any advantage with respect to a monodispersed type of clustering, we performed Monte Carlo simulations, varying the number of receptors per cluster, assuming that the cluster size depends linearly on the number of receptors per cluster (supplemental Fig. S3*D*). As expected, the presence of clusters formed by a larger number of receptors progressively shifted the *ccdf* decay toward larger n (Fig. 7*C*). Interestingly, the *ccdf* obtained for the experimental distribution of n_{clust} (*black curve*) initially follows the same behavior as that simulated for $n_{\text{clust}} = 3$, to then decay similarly as $n_{\text{clust}} = 5$ and finally overlapping with the *ccdf* simulated for $n_{\text{clust}} = 8$. Therefore, these simulations show that the heterogeneity experimentally observed for the molecular density of DC-SIGN nanoclusters might serve to effectively broaden its binding capabilities to a variety of viruses having different sizes and/or binding affinities for DC-SIGN. Lateral mobility of nanoclusters, as observed in our experiments, will then further virus capture by increasing the probability of encountering events.

DISCUSSION

It has been extensively documented that DC-SIGN forms stable tetramers both *in vitro* and in living cells (21–23, 37). Tetramers would allow the establishment of multivalent interactions via the CRDs, increasing the adhesion energy of DC-SIGN to its ligands. Our results now show a higher level of spatial complexity of DC-SIGN at the cell membrane and demonstrate for the first time a direct structural relationship between tetramer stability and nanoclustering formation sustained by the neck region of DC-SIGN. Furthermore, this particular arrangement appeared crucial for efficient binding of nanometer scale pathogens, such as viruses, underscoring a physiological role for nanoclustering. Thus, our work provides a clear example of self-organization at the cell surface prior to ligand activation that is driven by the molecular structure of the receptor.

It has been proposed that the extended and flexible structure of the DC-SIGN neck region might play a role in favorably positioning the CRDs for efficient pathogen binding (21, 22) and that neck-truncated molecules did not bind to HIV-1 because they are too short to emerge from the plasma membrane (30). Our binding assays show that the CRD of the neck-truncated mutant is fully available for binding to both soluble ligands and micrometer-sized objects and that the impaired binding to virus-like particles is mostly due to the lack of nanocluster spatial organization of DC-SIGN. We also observed that DC-SIGN-mediated internalization was independent of the neck region but highly affected by the cytoplasmic tail of DC-SIGN. These results thus reflect different functional properties of DC-SIGN directly related to its molecular structure (*i.e.* whereas nanoclustering is important for pathogen binding, the cytoplasmic region determines internalization efficiency).

Recent work using diffraction-limited confocal imaging showed that on imDCs and fibroblast cell lines, DC-SIGN form immobile *microdomains* of dimensions larger than 600 nm stabilized by interactions between the CRDs and the extracellular matrix (26–28). Deletion of the CRD abrogated *microclustering* and resulted in DC-SIGN lateral diffusion on the cell membrane, as measured by fluorescence recovery after photobleaching using full Abs (28). In apparent contrast, we observed that truncation of the CRDs did not affect the *nanoclustering* capacity of DC-SIGN and that nanoclusters are fully mobile, independent of the cell type and mutant investigated. Because of the limited spatial resolution of confocal microscopy, it might well be that nanoclusters (of sizes <180 nm as observed in our superresolution experiments) spatially proximal to each other appear as larger clusters when inspected by confocal microscopy. Indeed, recent work from the same group using superresolution blink microscopy showed that the microdomains observed by diffraction-limited optical techniques are in fact composed of discrete DC-SIGN nanodomains (40). In addition, receptor diffusion measurements on the cell membrane are highly influenced by the labeling conditions. Whereas the use of full Abs might induce cross-linking of close by receptors increasing clustering beyond the native state and reducing their overall mobility to the level of fixed cells (41, 42), single chains or Fabs, as used in our experiments, guarantee that both nanoclustering and lateral mobility are minimally influenced. Additionally, possible Ab-induced receptor cross-linking could contribute to initiate DC-SIGN endocytosis via nascent clathrin-coated pits. These nascent endocytic complexes are likely to appear as immobile features at the observed time scale.

In summary, we have shown that homophilic interactions mediated by the neck region of DC-SIGN are essential to coordinate its spatiotemporal organization on the cell membrane, effectively broadening its binding capabilities to nanoscale-sized pathogens. Because lateral mobility of receptors and ligands plays a key role in facilitating mutual interactions, our results indicate that for a given number of receptors at the cell surface, tight spatial coordination in nanoclusters guarantees highly energetic interactions with ligands, whereas lateral mobility enhances the probability of encountering the ligand for effective binding.

Interestingly, different DC-SIGN neck variants have been found to naturally occur on dendritic and myeloid cells (37), and polymorphisms in the DC-SIGN gene affecting the length of the neck region appeared to be correlated with altered susceptibility to HIV infection (43, 44). Also with HIV, DC-SIGN is known to interact with a plethora of viruses with different sizes and properties. Whereas DC-SIGN has been shown to solely act as an attachment factor for viruses such as ebola (45), measles (46), and hepatitis C (47), recent publications have demonstrated the direct involvement of DC-SIGN in the entry of viruses, such as arthropod-borne phleboviruses (48), coronavirus (49), and human herpesvirus 8 (50). Clearly, DC-SIGN binds with equal efficiency to viruses of different sizes (from Dengue (~50 nm) to HIV (~100 nm) and measles virus (200–300 nm)). Our group has already shown that DC-SIGN is able to bind to gp120-coated particles of 40 nm in size as well as real HIV virions (11). In addition, Pohlmann *et al.* (30) have reported that real HIV virus cannot bind to DC-SIGN-ΔRep, implying that 40 nm and 100 nm are equally not bound by this mutant. Our work therefore demonstrates that the plasticity of DC-SIGN virus binding capacity is largely determined by its variable nanoclustering capacity, which is regulated by the neck region of the receptor. Furthermore, our simulations indicate that the number of receptors included in the clusters defines the effectiveness of the binding as long as the sizes of the viruses are comparable with the sizes of the DC-SIGN nanoclusters (*i.e.* from 80 to 400 nm with a mean size of 180 nm). Thus, the inherent nanoclustering of DC-SIGN driven by the neck region, as observed in our measurements, could have important implications for DC-SIGN functionality under physiological settings and impact our understanding of membrane receptor organization in relation to virus entry into the cells.

We recently demonstrated that ligand binding via the DC-SIGN neck region leads to prolonged antigen storage and enhanced cross-presentation capacity (43). Exploitation of the DC-SIGN neck region therefore represents an intriguing possibility for the development of novel targeted vaccination strategies, justifying the increasing interest in the contribution of the neck region to the immunobiology of DC-SIGN.

Acknowledgments—We thank O. Esteban for preparing the Fab fragments, A. Eek and T. Huijs for making the DC-SIGN mutants, M. Rivas for technical assistance, and S. Buschow for fruitful discussions. STED images were obtained at the Institut de Ciencies Fotoniques Super-Resolution Light Nanoscopy Facility, SLN@ICFO. We gratefully thank D. L. Williams for providing the Alexa-labeled mannan from C. albicans.

REFERENCES

1. Banchereau, J., and Steinman, R. M. (1998) Dendritic cells and the control of immunity. *Nature* **392,** 245–252
2. Steinman, R. M. (1991) The dendritic cell system and its role in immunogenicity. *Annu. Rev. Immunol.* **9,** 271–296
3. Théry, C., and Amigorena, S. (2001) The cell biology of antigen presentation in dendritic cells. *Curr. Opin. Immunol.* **13,** 45–51
4. Trombetta, E. S., and Mellman, I. (2005) Cell biology of antigen processing *in vitro* and *in vivo*. *Annu Rev. Immunol.* **23,** 975–1028
5. Cambi, A., and Figdor, C. G. (2003) Dual function of C-type lectin-like receptors in the immune system. *Curr. Opin. Cell Biol.* **15,** 539–546
6. van Kooyk, Y., and Geijtenbeek, T. B. (2003) DC-sign. Escape mechanism for pathogens. *Nat. Rev. Immunol.* **3,** 697–709
7. Tacken, P.J., de Vries, I. J., Torensma, R., and Figdor, C. G. (2007) Dendritic cell immunotherapy. From *ex vivo* loading to *in vivo* targeting. *Nat. Rev. Immunol.* **7,** 790–802
8. Bonifaz, L. C., Bonnyay, D. P., Charalambous, A., Darguste, D. I., Fujii, S., Soares, H., Brimnes, M. K., Moltedo, B., Moran, T. M., and Steinman, R. M. (2004) *In vivo* targeting of antigens to maturing dendritic cells via the DEC-205 receptor improves T cell vaccination. *J. Exp. Med.* **199,** 815–824
9. Geijtenbeek, T. B., Krooshoop, D. J., Bleijs, D. A., van Vliet, S. J., van Duijnhoven, G. C., Grabovsky, V., Alon, R., Figdor, C. G., and van Kooyk, Y. (2000) DC-SIGN-ICAM-2 interaction mediates dendritic cell trafficking. *Nat. Immunol.* **1,** 353–357
10. Soilleux, E. J., Morris, L. S., Leslie, G., Chehimi, J., Luo, Q., Levroney, E., Trowsdale, J., Montaner, L. J., Doms, R. W., Weissman, D., Coleman, N., and Lee, B. (2002) Constitutive and induced expression of DC-SIGN on dendritic cell and macrophage subpopulations *in situ* and *in vitro*. *J. Leukoc. Biol.* **71,** 445–457
11. Cambi, A., de Lange, F., van Maarseveen, N. M., Nijhuis, M., Joosten, B., van Dijk, E. M., de Bakker, B. I., Fransen, J. A., Bovee-Geurts, P. H., van Leeuwen, F. N., Van Hulst, N. F., Figdor, C. G. (2004) Microdomains of the C-type lectin DC-SIGN are portals for virus entry into dendritic cells. *J. Cell Biol.* **164,** 145–155
12. Puig-Kröger, A., Serrano-Gómez, D., Caparrós, E., Domínguez-Soto, A., Relloso, M., Colmenares, M., Martínez-Muñoz, L., Longo, N., Sánchez-Sánchez, N., Rincon, M., Rivas, L., Sánchez-Mateos, P., Fernández-Ruiz, E., and Corbí, A. L. (2004) Regulated expression of the pathogen receptor dendritic cell-specific intercellular adhesion molecule 3 (ICAM-3)-grabbing nonintegrin in THP-1 human leukemic cells, monocytes, and macrophages. *J. Biol. Chem.* **279,** 25680–25688
13. Geijtenbeek, T. B., Kwon, D. S., Torensma, R., van Vliet, S. J., van Duijnhoven, G. C., Middel, J., Cornelissen, I. L., Nottet, H. S., KewalRamani, V. N., Littman, D. R., Figdor, C. G., and van Kooyk, Y. (2000) DC-SIGN, a dendritic cell-specific HIV-1-binding protein that enhances trans-infection of T cells. *Cell* **100,** 587–597
14. Alvarez, C. P., Lasala, F., Carrillo, J., Muñiz, O., Corbí, A. L., and Delgado, R. (2002) C-type lectins DC-SIGN and L-SIGN mediate cellular entry by ebola virus in cis and in trans. *J. Virol.* **76,** 6841–6844
15. Ludwig, I. S., Lekkerkerker, A., N., Depla, E., Bosman, F., Musters, R. J., Depraetere, S., van Kooyk, Y., and Geijtenbeek, T. B. (2004) Hepatitis C virus targets DC-SIGN and L-SIGN to escape lysosornal degradation. *J. Virol.* **78,** 8322–8332
16. Cambi, A., Gijzen, K., de Vries, J. M., Torensma, R., Joosten, B., Adema, G. J., Netea, M. G., Kullberg, B. J., Romani, L., Figdor, C. G. (2003) The C-type lectin DC-SIGN (CD209) is an antigen-uptake receptor for *Candida albicans* on dendritic cells. *Eur. J. Immunol.* **33,** 532–538
17. Geijtenbeek, T. B., van Vliet, S. J., Koppel, E. A., Sanchez-Hernandez, M., Vandenbroucke-Grauls, C. M., Appelmelk, B., and Van Kooyk, Y. (2003) Mycobacteria target DC-SIGN to suppress dendritic cell function. *J. Exp. Med.* **197,** 7–17
18. Gringhuis, S. I., den Dunnen, J., Litjens, M., van der Vlist, M., and Geijtenbeek, T. B. (2009) Carbohydrate-specific signaling through the DC-SIGN signalosome tailors immunity to *Mycobacterium tuberculosis*, HIV-1 and *Helicobacter pylori*. *Nat. Immunol.* **10,** 1081–1088
19. Feinberg, H., Mitchell, D. A., Drickamer, K., Weis, W. I. (2001) Structural basis for selective recognition of oligosaccharides by DC-SIGN and DC-SIGNR. *Science* **294,** 2163–2166
20. Mitchell, D. A., Fadden, A. J., and Drickamer, K. (2001) A novel mechanism of carbohydrate recognition by the C-type lectins DC-SIGN and DC-SIGNR. Subunit organization and binding to multivalent ligands. *J. Biol. Chem.* **276,** 28939–28945
21. Feinberg, H., Guo, Y., Mitchell, D. A., Drickamer, K., Weis, W. I. (2005) Extended neck regions stabilize tetramers of the receptors DC-SIGN and DC-SIGNR. *J. Biol. Chem.* **280,** 1327–1335
22. Yu, Q. D., Oldring, A. P., Powlesland, A. S., Tso, C. K., Yang, C., Drickamer, K., and Taylor, M. E. (2009) Autonomous tetramerization domains in the glycan-binding receptors DC-SIGN and DC-SIGNR. *J. Mol. Biol.* **387,** 1075–1080
23. Menon, S., Rosenberg, K., Graham, S. A., Ward, E. M., Taylor, M. E., Drickamer, K., and Leckband, D. E. (2009) Binding-site geometry and flexibility in DC-SIGN demonstrated with surface force measurements. *Proc. Natl. Acad. Sci. U.S.A.* **106,** 11524–11529
24. Koopman, M., Cambi, A., de Bakker, B. I., Joosten, B., Figdor, C. G., van Hulst, N. F., and Garcia-Parajo, M. F. (2004) Near-field scanning optical microscopy in liquid for high resolution single molecule detection on dendritic cells. *FEBS Lett.* **573,** 6–10
25. de Bakker, B., I., de Lange, F., Cambi, A., Korterik, J. P., van Dijk, E. M., van Hulst, N. F., Figdor, C. G., and Garcia-Parajo, M. F. (2007) Nanoscale organization of the pathogen receptor DC-SIGN mapped by single-molecule high-resolution fluorescence microscopy. *Chemphyschem* **8,** 1473–1480
26. Neumann, A. K., Thompson, N. L., and Jacobson, K. (2008) Distribution and lateral mobility of DC-SIGN on immature dendritic cells. Implications for pathogen uptake. *J. Cell Sci.* **121,** 634–643
27. Itano, M. S., Neumann, A. K., Liu, P., Zhang, F., Gratton, E., Parak, W. J., Thompson, N. L., and Jacobson, K. (2011) DC-SIGN and influenza hemagglutinin dynamics in plasma membrane microdomains are markedly different. *Biophys. J.* **100,** 2662–2670
28. Liu, P., Wang, X., Itano, M. S., Neumann, A. K., Jacobson, K., and Thompson, N. L. (2012) The formation and stability of DC-SIGN microdomains

require its extracellular moiety. *Traffic* **13,** 715–726

29. Geijtenbeek, T. B., Torensma, R., van Vliet, S. J., van Duijnhoven, G. C., Adema, G. J., van Kooyk, Y., and Figdor, C. G. (2000) Identification of DC-SIGN, a novel dendritic cell-specific ICAM-3 receptor that supports primary immune responses. *Cell* **100,** 575–585
30. Pohlmann, S., Leslie, G. J., Edwards, T. G., Macfarlan, T., Reeves, J. D., Hiebenthal-Millow, K., Kirchhoff, F., Baribaud, F., and Doms, R. W. (2001) DC-SIGN interactions with human immunodeficiency virus. Virus binding and transfer are dissociable functions. *J. Virol.* **75,** 10523–10526
31. Tacken, P. J., Ginter, W., Berod, L., Cruz, L. J., Joosten, B., Sparwasser, T., Figdor, C. G., and Cambi, A. (2011) Targeting DC-SIGN via its neck region leads to prolonged antigen residence in early endosomes, delayed lysosomal degradation, and cross-presentation. *Blood* **118,** 4111–4119
32. Sierra-Filardi, E., Estecha, A., Samaniego, R., Fernández-Ruiz, E., Colmenares, M., Sánchez-Mateos, P., Steinman, R. M., Granelli-Piperno, A., and Corbí, A. L. (2010) Epitope mapping on the dendritic cell-specific ICAM-3-grabbing non-integrin (DC-SIGN) pathogen-attachment factor. *Mol. Immunol.* **47,** 840–848
33. Cambi, A., Beeren, I., Joosten, B., Fransen, J. A., and Figdor, C. G. (2009) The C-type lectin DC-SIGN internalizes soluble antigens and HIV-1 virions via a clathrin-dependent mechanism. *Eur. J. Immunol.* **39,** 1923–1928
34. Cambi, A., Lidke, D. S., Arndt-Jovin, D. J., Figdor, C. G., and Jovin, T. M. (2007) Ligand-conjugated quantum dots monitor antigen uptake and processing by dendritic cells. *Nano Lett.* **7,** 970–977
35. Zhu, P., Chertova, E., Bess, J., Jr., Lifson, J. D., Arthur, L. O., Liu, J., Taylor, K. A., and Roux, K. H. (2003) Electron tomography analysis of envelope glycoprotein trimers on HIV and simian immunodeficiency virus virions. *Proc. Natl. Acad. Sci. U.S.A.* **100,** 15812–15817
36. Smith, A. L, Ganesh, L., Leung, K., Jongstra-Bilen, J., Jongstra, J., and Nabel, G. J. (2007) Leukocyte-specific protein 1 interacts with DC-SIGN and mediates transport of HIV to the proteasome in dendritic cells. *J. Exp. Med.* **204,** 421–430
37. Serrano-Gómez, D., Sierra-Filardi, E., Martínez-Nuñez, R. T., Caparrós, E., Delgado, R., Muñoz-Fernández, M. A., Abad, M. A., Jimenez-Barbero, J., Leal, M., and Corbí, A. L. (2008) Structural requirements for multimerization of the pathogen receptor dendritic cell-specific ICAM3-grabbing non-integrin (CD209) on the cell surface. *J. Biol. Chem.* **283,** 3889–3903
38. Chung, I., Akita, R., Vandlen, R., Toomre, D., Schlessinger, J., and Mellman, I. (2010) Spatial control of EGF receptor activation by reversible dimerization on living cells. *Nature* **464,** 783–787
39. Bakker, G. J., Eich, C., Torreno-Pina, J. A., Diez-Ahedo, R., Perez-Samper, G., van Zanten, T. S., Figdor, C. G., Cambi, A., and Garcia-Parajo, M. F. (2012) Lateral mobility of individual integrin nanoclusters orchestrates the onset for leukocyte adhesion. *Proc. Natl. Acad. Sci. U.S.A.* **109,** 4869–4874
40. Itano, M. S., Steinhauer, C., Schmied, J. J., Forthmann, C., Liu, P., Neumann, A. K., Thompson, N. L., Tinnefeld, P., and Jacobson, K. (2012) Super-resolution imaging of C-type lectin and influenza hemagglutinin nanodomains on plasma membranes using blink microscopy. *Biophys. J.* **102,** 1534–1542
41. Gaborski, T. R., Clark, A., Waugh, R. E., and McGrath, J. L. (2008) Membrane mobility of β2 integrins and rolling associated adhesion molecules in resting neutrophils. *Biophys. J.* **95,** 4934–4947
42. Ashby, M. C., Maier, S. R., Nishimune, A., and Henley, J. M. (2006) Lateral diffusion drives constitutive exchange of AMPA receptors at dendritic spines and is regulated by spine morphology. *J. Neurosci.* **26,** 7046–7055
43. Liu, H., L., Hladik, F., Andrus, T., Sakchalathorn, P., Lentz, G. M., Fialkow, M. F., Corey, L., McElrath, M. J., and Zhu, T. (2005) Most DC-SIGNR transcripts at mucosal HIV transmission sites are alternatively spliced isoforms. *Eur. J. Hum. Genet.* **13,** 707–715
44. Khoo, U. S., Chan, K. Y., Chan, V. S., and Lin, C. L. (2008) DC-SIGN and L-SIGN. The SIGNs for infection. *J. Mol. Med.* **86,** 861–874
45. Simmons, G., Reeves, J. D., Grogan, C. C., Vandenberghe, L. H., Baribaud, F., Whitbeck, J. C., Burke, E., Buchmeier, M. J., Soilleux, E. J., Riley, J. L., Doms, R. W., Bates, P., and Pöhlmann, S (2003) DC-SIGN and DC-SIGNR bind ebola glycoproteins and enhance infection of macrophages and endothelial cells. *Virology* **305,** 115–123
46. de Witte, L., Abt, M., Schneider-Schaulies, S., van Kooyk, Y., and Geijtenbeek, T. B. (2006) Measles virus targets DC-SIGN to enhance dendritic cell infection. *J. Virol.* **80,** 3477–3486
47. Lozach, P. Y., Amara, A., Bartosch, B., Virelizier, J. L., Arenzana-Seisdedos, F., Cosset, F. L., and Altmeyer, R. (2004) C-type lectins L-SIGN and DC-SIGN capture and transmit infectious hepatitis C virus pseudotype particles. *J. Biol. Chem.* **279,** 32035–32045
48. Lozach, P., Y., Kühbacher, A., Meier, R., Mancini, R., Bitto, D., Bouloy, M., and Helenius, A. (2011) DC-SIGN as a receptor for phleboviruses. *Cell Host Microbe.* **10,** 75–88
49. Regan, A. D., and Whittaker, G. R. (2008) Utilization of DC-SIGN for entry of feline coronaviruses into host cells. *J. Virol.* **82,** 11992–11996
50. Rappocciolo, G., Hensler, H. R., Jais, M., Reinhart, T. A., Pegu, A., Jenkins, F. J., and Rinaldo, C. R. (2008) Human herpesvirus 8 infects and replicates in primary cultures of activated B lymphocytes through DC-SIGN. *J. Virol.* **82,** 4793–4806